

Inverse Scattering via Transmission Matrices: Broadband Illumination and Fast Phase Retrieval Algorithms

Manoj Kumar Sharma*, Christopher A. Metzler*, Sudarshan Nagesh, Richard G. Baraniuk, Oliver Cossairt, Ashok Veeraraghavan

Abstract—When a narrowband coherent wavefront passes through or reflects off of a scattering medium, the input and output relationship of the incident field is linear and so can be described by a transmission matrix (TM). If the TM for a given scattering medium is known, one can computationally “invert” the scattering process and image through the medium. In this work, we investigate the effect of broadband illumination, i.e., what happens when the wavefront is only partially coherent? Can one still measure a TM and “invert” the scattering?

To accomplish this task, we measure TMs using the double phase retrieval technique, a method which uses phase retrieval algorithms to avoid difficult-to-capture interferometric measurements. Generally, using the double phase retrieval method requires performing massive amounts of computation. We alleviate this burden by developing a fast, GPU-accelerated algorithm, prVAMP, which lets us reconstruct $256^2 \times 64^2$ TMs in under five hours.

After reconstructing several TMs using this method, we find that, as expected, reducing the coherence of the illumination significantly restricts our ability to invert the scattering process. Moreover, we find that past a certain bandwidth an incoherent, intensity-based scattering model better describes the scattering process and is easier to invert.

Index Terms—Transmission Matrix, Phase Retrieval, Scattering.

I. INTRODUCTION

At first glance, imaging through multiple-scattering media seems like an impossible task. Any light incident on the media will undergo multiple reflections. Thus, if we illuminate an object with coherent light, the resulting wavefront will constructively and destructively interfere with itself, and a speckle pattern will be produced on the far side of the scatterer. This speckle pattern generally bears no resemblance to the original image.

A. Inverse Scattering is the Holy Grail of Imaging

Despite the challenge inherent to imaging through scattering media, it is a crucial problem within the optics community. Imaging through scattering media is fundamental to numerous applications including imaging through biological tissues, long-distance imaging through smog, fog, etc., imaging

through the atmosphere, and more. Accordingly, numerous attempts have been made to solve the inverse scattering problem. We list some of them next.

B. Imaging Through Scattering Media Today

Confocal microscopy [1], [2] mitigates the scattering effect by using a pinhole to ignore scattered, out-of-focus light. The performance of this method is limited to few attenuation lengths of scatterings and requires very slow, scanned image acquisitions.

Time and/or coherence-gating techniques [3], [4], [5], [6], [7], [8] rely upon the fact that a scattered photon is unlikely to arrive at the same time as a ballistic photon; a photon that went to the target and back without scattering. As a result, one can use pulsed illumination and temporal/coherence gating to separate the ballistic photons from a region of interest. Gating is well-suited to rapidly changing scatterers, like fog, and as it offers rapid acquisition times and does not require the scattering process to be stable over time. However, because these systems only measure ballistic photons, they require powerful and expensive pulsed lasers to image through thick scatterers.

Multi-slice light propagation [9], [10], [11] is another method to image through scattering media. As the name suggests, the multi-slice light-propagation method models a scattering material as a series of 2D scattering slices between which light propagates. Rather than blindly mapping inputs to outputs, the multi-slice propagation method learns a composition of linear transformations. This method is uniquely suited to perform 3D reconstructions; moreover, it provides information about the actual structure of the scattering material. However, the multi-slice approach does not model reflections within the scatterer, and it is unclear how well this method works with thick scattering materials.

Recently phase retrieval techniques are used for wavefront sensing through thin scattering media[[12]] and to image rough distant objects [13], [14], however, when dealing with thin scattering media, single-shot imaging through scattering media is possible using memory-effect based techniques [15], [16]. These methods assume that the scattering medium preserves the strong angular correlation of the speckle patterns; which implies that, with temporally coherent and spatially incoherent illumination, the scattering process follows a convolution model with a speckle-like point spread function. From there

M. Sharma, C. Metzler, R. Baraniuk, and A. Veeraraghavan are with the Department of Electrical and Computer Engineering, Rice University, Houston, TX, 77005 USA e-mail: imaging.mks@gmail.com.

S. Nagesh and O. Cossairt are with Northwestern University, Evanston, IL, 60208 USA.

*M. Sharma and C. Metzler contributed equally.

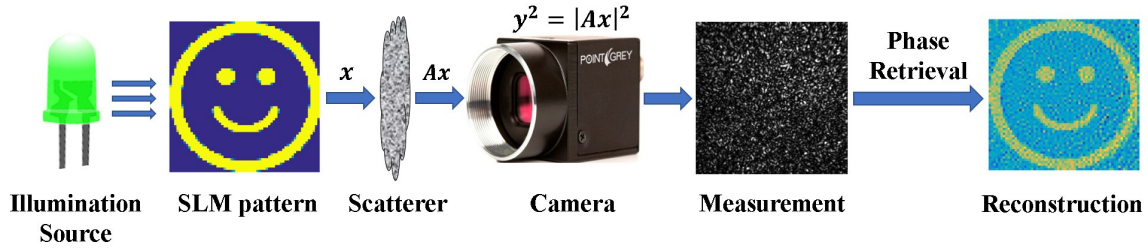


Fig. 1. A sketch of our experimental setup. An illumination source is modulated by an SLM to form a smiley face, the light field scatters and produces a speckle pattern, the intensity of the speckle pattern is measured by a camera, and we use phase retrieval algorithms to reconstruct the smiley face from the speckle pattern.

one can invert the scattering process by estimating the target's auto-correlation function and then performing phase retrieval. This method fails when the scattering medium becomes too thick for the strong memory effect to hold.

C. Transmission Matrices

The gold standard to image through very *thick* and *stable* scattering media is inverse scattering with optical transmission matrices (TMs). Unlike many of the aforementioned methods, inverse scattering with TMs does not require any ballistic photons and the scattering media does not need to exhibit the memory effect. However, TM methods need the scattering media's behavior to be invariant over time; TM techniques are not well-suited to dynamic media like fog. Moreover, TM methods generally assume that you have access to the far side of the scattering media for calibration, which allows you to characterize the relation between the input field, on a spatial light modulator (SLM), and the output field, on a camera.

TM methods are based upon the principle that when dealing with coherent light, the forward scattering process is linear with respect to fields, and so the output field is related to the input field by a matrix \mathbf{A} . This matrix is called the TM. If one first measures the TM, one can then “invert” the scattering process and image through [17] or even inside [18] the scattering medium, potentially through the use of phase retrieval algorithms [19]. The imaging process is illustrated in Figure 1.

D. Multi-spectral Transmission Matrices

Traditionally, TMs describe the scattering process when dealing with coherent narrowband light, which lets you ignore the fact that scattering media have spectrally dependent responses [20]. In a recent work [20], the authors demonstrated that characterizing scattering with multi-spectral light is also possible. The key idea is to replace the 2D TM that describes the scattering process at a fixed wavelength, with a 3D tensor, which describes the scattering process at multiple wavelengths. This characterization enables temporal, as well as spatial, focusing through the scattering media [21].

E. Contributions: Measuring the Effects of Temporal Coherence and a Fast Phase Retrieval Algorithm

In this work, we study how effective a single TM is at characterizing and inverting the scattering process associated

with a broadband (i.e., partially coherent) illumination source. In essence, we study how well the narrow-band model can approximate a broadband system. We show that as the bandwidth of the illumination increases, the singular values of the measured TM decay towards zero and the speckle encodes less and less information. As the bandwidth increases, we quickly reach a point at which an incoherent scattering model better describes the scattering process and is easier to invert.

To carry out this task efficiently, we learn TMs using the double phase retrieval technique [22], [19]. This method uses phase retrieval algorithms to avoid difficult-to-capture interferometric measurements. Unfortunately, existing double phase retrieval methods require a massive amount of computation. In this work we have developed a fast, GPU-accelerated algorithm which lets us reconstruct $256^2 \times 64^2$ TMs in under five hours, as opposed to the tens of thousands that would be required with competing methods. An initial version of this algorithm was presented in [23].

II. MODELING SCATTERING

In this section, we describe the models underlying TM-based methods.

A. Narrow-band Illumination

When dealing with completely coherent light, the scattering process is linear with respect to *complex-valued* fields. Thus, the complex field \mathbf{z} on the far side of the scattering media is related to the field \mathbf{x} incident on the scattering media via the *complex-valued monochromatic transmission matrix* \mathbf{A} .

That is,

$$\mathbf{z} = \mathbf{A}\mathbf{x} + \epsilon_F, \quad (1)$$

where ϵ_F models noise on the field.

Typical cameras capture only intensity information, in which case the measurement process becomes

$$\mathbf{y}^2 = |\mathbf{A}\mathbf{x} + \epsilon_F|^2 + \epsilon_I, \quad (2)$$

where the square is elementwise and ϵ_I models noise on the intensity measurement. In this work we ignore ϵ_I , which we minimize through long exposures and strong illumination, and also take the square root of the intensity measurements. Our simplified measurement model becomes

$$\mathbf{y} = |\mathbf{A}\mathbf{x} + \epsilon|. \quad (3)$$

After one measures the TM, potentially using the double phase retrieval method described in Section III-A, one can use phase retrieval algorithms to reconstruct a signal \mathbf{x} from measurements \mathbf{y} . Thus phase retrieval algorithms can be used to see through multiple-scattering media.

B. Incoherent Illumination

At the other extreme, with completely incoherent illumination the scattering process is linear with respect to *real-valued* intensities. That is,

$$\mathbf{y}^2 = \mathbf{A}_{\text{intensity}} \mathbf{x}^2 + \epsilon. \quad (4)$$

This makes reconstructing \mathbf{x}^2 from \mathbf{y}^2 , and thus imaging through scattering media, a simple least squares problem. Unfortunately, the *real-valued intensity transmission matrix* $\mathbf{A}_{\text{intensity}}$ tends to be very poorly conditioned.

C. Multi-spectral Illumination

If one is able to distinguish/measure the various spectral components of the input and output fields, one can form a *multi-spectral transmission matrix/tensor*, $\mathbf{A}(\omega_k)$ for $k = 1, \dots, K$, and model scattering as

$$\mathbf{z}(\omega_k) = \mathbf{A}(\omega_k) \mathbf{x}(\omega_k) + \epsilon(\omega_k), \quad (5)$$

for frequencies $\omega_1, \dots, \omega_K$. Multi-spectral TMs can enable spatio-temporal coherent control of broadband light [20], [21]. However, without access to narrow-band measurements, $\mathbf{A}(\omega_k)$ remains out of reach.

D. Broadband Illumination

For broadband illumination, where all frequency components are measured at once, the measurement process is best described by

$$\mathbf{y}^2 = \int |\mathbf{z}(\omega_k)|^2 d\omega_k = \int |\mathbf{A}(\omega_k) \mathbf{x}(\omega_k) + \epsilon(\omega_k)|^2 d\omega_k. \quad (6)$$

The intensities measured at the camera consist of the superposition of many different frequency components. However, without applying filters or otherwise capturing spectrally dependent measurements, these components are indistinguishable on the camera.

Thus, while ideally one would learn and invert $\mathbf{A}(\omega_k)$ across many frequencies, we are motivated to learn a single model for the scattering process and invert this. In effect, we approximate a broadband scattering model (6) using either coherent (2) or incoherent (4) models and study how well one can use said models to image through scattering media. For small illumination bandwidths, where the spectral bandwidth remains within the spectral memory effect [20], the coherent TM model should be quite accurate. However, as we increase the illumination bandwidth the measurements will have contributions from a diverse and uncorrelated set of narrow-band TMs and the model should break down. In contrast, increasing bandwidth should make the incoherent illumination model more accurate.

In the next section, we describe how we measure the coherent (complex-valued field) and incoherent (real-valued intensity) TMs, \mathbf{A} and $\mathbf{A}_{\text{intensity}}$.

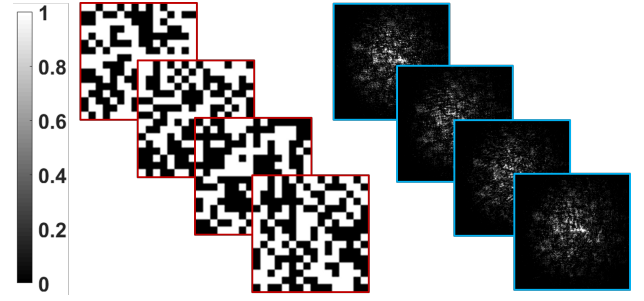


Fig. 2. Binary calibration patterns placed on the SLM and the corresponding measurements recorded by the camera. Random calibration patterns give rise to random uncorrelated speckle patterns.

III. MEASURING FIELD AND INTENSITY TRANSMISSION MATRICES

TMs are typically measured using holographic interferometry [24]. To learn a TM with interferometry, one illuminates one pixel of the SLM at a time. For each pixel, one uses interferometry to record the complex field incident on the detector. In this way, one is able to directly measure the TM, one column at a time.¹

While effective, interferometric methods are very sensitive to perturbations; even minute vibrations, such as those caused by an air conditioning unit turning on and off in a lab, can be enough to change the interference pattern and thereby kill this method. This problem becomes particularly pernicious at higher resolutions where the physical stability requirement becomes more and more demanding.

In this work, we avoid the challenge of accurately measuring complex-valued fields by using the double phase retrieval method [22], [19]. The key idea behind double phase retrieval is that if one measures a sufficient number of the intensities of responses to calibration signals, one can use phase retrieval algorithms to learn the TM.

In this section, we explain double phase retrieval and introduce a new, GPU-accelerated algorithm that vastly reduces the computation times associated with this method. We also briefly describe how we measure intensity TMs.

A. Double Phase Retrieval

The double phase retrieval method gets its name from the fact that it requires performing phase retrieval twice; once for calibration, i.e., measuring the TM, and once for imaging.

1) *Calibration*: One first sends a series of calibration patterns $\mathbf{x}_p \in \mathbb{R}^N$ with $p = 1, \dots, P$, through the scattering media, see Figure 2. For each p , the signal will be transformed by the TM $\mathbf{A} \in \mathbb{C}^{M \times N}$, to produce measurements $\mathbf{y}_p \in \mathbb{R}_+^M$, with

$$\mathbf{y}_p = |\mathbf{A} \mathbf{x}_p + \epsilon_p|,$$

where ϵ_p denotes noise.² Actual calibration patterns and their corresponding measurements are illustrated in Fig. 2.

¹This is not the only, nor best, way to measure a TM using interferometry. For instance, [25] more efficiently measures a TM by temporally modulating the phase of an SLM and capturing a video of a dynamic speckle pattern.

²Multiple sources of noise, for instance leakage across the SLM, contribute to the noise ϵ_p . In this work, we assume that ϵ_p follows a white circularly-symmetric complex Gaussian distribution.

The sets of calibration, measurement, and noise column vectors are then concatenated with themselves to form $\mathbf{X} = [\mathbf{x}_1, \mathbf{x}_2, \dots, \mathbf{x}_p] \in \mathbb{R}^{N \times P}$, $\mathbf{Y} = [\mathbf{y}_1, \mathbf{y}_2, \dots, \mathbf{y}_p] \in \mathbb{R}_+^{M \times P}$, and $\mathbf{E} = [\epsilon_1, \epsilon_2, \dots, \epsilon_p] \in \mathbb{C}^{M \times P}$.

In this way, the entire calibration process can be described by the equation

$$\mathbf{Y} = |\mathbf{A}\mathbf{X} + \mathbf{E}|.$$

Taking the transpose of the above equality, one obtains

$$\mathbf{Y}^H = |\mathbf{X}^H \mathbf{A}^H + \mathbf{E}^H|.$$

Consider the m^{th} column of \mathbf{Y}^H (this consists of the P measurements associated with the m^{th} detector pixel)

$$\mathbf{y}_m^H = |\mathbf{X}^H \mathbf{a}_m^H + \epsilon_m^H|, \quad (7)$$

where \mathbf{a}_m^H and ϵ_m^H denote the m^{th} rows of \mathbf{A} and \mathbf{E} .

Assuming P is sufficiently large (as a rule of thumb $P > 4N$), one can apply phase retrieval algorithms to (7) to recover each row \mathbf{a}_m^H ; simply treat \mathbf{y}_m^H as the measurement and \mathbf{X}^H as the measurement matrix. This can be repeated for each of the M rows of \mathbf{A} , potentially in parallel, to learn the entire TM.

2) *Imaging*: After one has an estimate $\tilde{\mathbf{A}}$ of the TM, imaging through the scattering medium is straightforward. Given a speckle pattern \mathbf{y} , one needs only apply phase retrieval algorithms to the measurements with $\tilde{\mathbf{A}}$ as the known measurement matrix.

B. prVAMP: A Fast and Robust Phase Retrieval Algorithm

The central challenge to using the double phase retrieval method in practice is computation times. Experimental systems often have low signal to noise ratios and when using an amplitude SLM the measurement matrix \mathbf{X}^H is nonzero mean.³ In this context, especially at low sampling rates, few phase retrieval algorithms perform accurate reconstructions. Unfortunately, the algorithm that works by far the best, prSAMP [26], is extremely slow; reconstructing one row of a $256^2 \times 64^2$ TM with prSAMP takes over an hour.

One way to reduce these computation times is to use special block-diagonal measurement matrices, but this comes at a cost in terms of recovery accuracy [27]. We propose a complementary solution.

In this work, we develop a new algorithm, prVAMP, which offers the same accuracy as prSAMP, while running hundreds of times faster. Simulations comparing prVAMP with over a dozen other phase retrieval algorithms are provided in Appendix A. In Appendix B we compare prVAMP and prSAMP with and without the fast, block-diagonal matrices from [27].

prVAMP is a special case of the recently developed Generalized Vector Approximate Message Passing (GVAMP) [28] algorithm. GVAMP is an algorithm for computing approximate minimum means squared error (MMSE) or maximum a posteriori (MAP) solutions to inverse problems involving

³In our experiments, the elements of \mathbf{X}^H are i.i.d. Bernoulli distributed with $p = .5$. I.e., each element of \mathbf{X} is 0 or 1, each with probability 0.5.

Algorithm 1 prVAMP

```

1: Initialize:  $\mathbf{r}_{10}, \mathbf{p}_{10}, \gamma_{10}, \tau_{10}$ 
2: for  $k=0, 1, \dots, K$  do
3:   Denoise  $\mathbf{x}$ :
4:    $\hat{\mathbf{x}}_{1,k} = g_{x1}(\mathbf{r}_{1,k}, \gamma_{1,k})$ ,
5:    $\alpha_{1,k} = \langle g'_{x1}(\mathbf{r}_{1,k}, \gamma_{1,k}) \rangle$ 
6:    $\mathbf{r}_{2k} = (\hat{\mathbf{x}}_{1,k} - \alpha_{1,k} \mathbf{r}_{1k}) / (1 - \alpha_{1,k})$ ,
7:    $\gamma_{2k} = \gamma_{1k} (1 - \alpha_{1,k}) / \alpha_{1k}$ 
8:   Denoise  $\mathbf{z}$ :
9:    $\hat{\mathbf{z}}_{1,k} = g_{z1}(\mathbf{p}_{1k}, \tau_{1k})$ ,
10:   $\beta_{1k} = \langle g'_{z1}(\mathbf{p}_{1k}, \tau_{1k}) \rangle$ 
11:   $\mathbf{p}_{2k} = (\hat{\mathbf{z}}_{1,k} - \beta_{1k} \mathbf{p}_{1k}) / (1 - \beta_{1k})$ ,
12:   $\tau_{2k} = \tau_{1k} (1 - \beta_{1k}) / \beta_{1k}$ 
13:  LMMSE estimation of  $\mathbf{x}$ :
14:   $\hat{\mathbf{x}}_{2k} = g_{x2}(\mathbf{r}_{2k}, \mathbf{p}_{2k}, \gamma_{2k}, \tau_{2k})$ ,
15:   $\alpha_{2k} = \langle g'_{x2}(\mathbf{r}_{2k}, \mathbf{p}_{2k}, \gamma_{2k}, \tau_{2k}) \rangle$ 
16:   $\mathbf{r}_{1,k+1} = (\hat{\mathbf{x}}_{2k} - \alpha_{2k} \mathbf{r}_{2k}) / (1 - \alpha_{2k})$ ,
17:   $\gamma_{1,k+1} = \gamma_{2k} (1 - \alpha_{2k}) / \alpha_{2k}$ 
18:  LMMSE estimation of  $\mathbf{z}$ :
19:   $\hat{\mathbf{z}}_{2k} = g_{z2}(\mathbf{r}_{2k}, \mathbf{p}_{2k}, \gamma_{2k}, \tau_{2k})$ ,
20:   $\beta_{2k} = \langle g'_{z2}(\mathbf{r}_{2k}, \mathbf{p}_{2k}, \gamma_{2k}, \tau_{2k}) \rangle$ 
21:   $\mathbf{p}_{1,k+1} = (\hat{\mathbf{z}}_{2k} - \beta_{2k} \mathbf{p}_{2k}) / (1 - \beta_{2k})$ ,
22:   $\tau_{1,k+1} = \tau_{2k} (1 - \beta_{2k}) / \beta_{2k}$ 
23: Return  $\hat{\mathbf{x}}_{1K}$ .
```

generalized linear measurements (GLMs); defined to be any measurement of the form

$$\mathbf{y} = Q(\mathbf{z} + \mathbf{w}) \text{ with } \mathbf{z} = \Phi \mathbf{x}, \quad (8)$$

where Φ is our measurement matrix (which is a known pattern \mathbf{X}^H when calibrating and an estimated TM $\tilde{\mathbf{A}}$ when imaging), \mathbf{x} is our signal of interest, \mathbf{w} is noise, and $Q(\cdot)$ denotes a simple non-linearity. prVAMP is designed for the special case $Q(\cdot) = |\cdot|$.

GVAMP can be broadly understood as an extension to GAMP [29], [30], which infuses the ADMM [31] concept of variable splitting into the algorithm. This modification allows GVAMP to handle non-zero-mean, correlated, and ill-conditioned measurement matrices, which would destabilize the original GAMP algorithm [32], [33].

The pseudo-code for prVAMP is presented in Algorithm 1. prVAMP works by first splitting the vectors \mathbf{x} and \mathbf{z} into two sets of identical vectors \mathbf{x}_1 and \mathbf{x}_2 and \mathbf{z}_1 and \mathbf{z}_2 . Iterations of the algorithm then broadly consist of four steps: First, there are two “denoising” steps which impose priors on \mathbf{x} and \mathbf{z} and ensure they are consistent with the measurements \mathbf{y} . Second, there are two linear minimum mean squared error (LMMSE) estimation steps which ensure the estimates of \mathbf{x} and \mathbf{z} are consistent with each other. Within the algorithm $\hat{\mathbf{x}}$ and $\hat{\mathbf{z}}$ terms are estimates of \mathbf{x} and \mathbf{z} , \mathbf{r} and \mathbf{p} terms act as noisy observations of \mathbf{x} and \mathbf{z} , the γ and τ terms track precisions (reciprocals of variances), and the α and β terms are divergence terms used to estimate these precisions.

We now give explicit forms for the various denoising and estimation functions listed in Algorithm 1. These expressions correspond to the MMSE form of the algorithm under i.i.d. Gaussian priors on the signal and noise. In all these

expressions we have dropped the iteration subscript k for readability.

1) *Denoising Steps*: On line 5 the algorithm denoises the noisy estimate \mathbf{r}_1 of the signal \mathbf{x} with the function $g_{x1}(\cdot)$; that is, it treats \mathbf{r}_1 as noisy observation of \mathbf{x} with additive white Gaussian noise with variance $1/\gamma_1$ and computes the MMSE estimate. When we a priori assume that \mathbf{x} is drawn from an i.i.d. zero-mean Gaussian distribution with variance $1/\tau_x$, this function becomes

$$g_{x1}(\mathbf{r}_1, \gamma_1) = \mathbb{E}[\mathbf{x}|\mathbf{r}_1, \gamma_1] = \frac{\gamma_1}{\gamma_x + \gamma_1} \mathbf{r}_1. \quad (9)$$

With the aforementioned assumptions on the distributions, $g_{x1}(\mathbf{r}_1, \gamma_1)$ just scales \mathbf{r}_1 . An expression for the average partial derivative $\langle g'_{x1}(\cdot) \rangle$ can be found in [29].

On line 10 the algorithm denoises the noisy estimate \mathbf{p}_1 of the signal \mathbf{z} with the function $g_{z1}(\cdot)$; that is, it treats \mathbf{p}_1 as noisy observation of \mathbf{z} with additive white Gaussian noise with variance $1/\tau_1$ and computes the elementwise MMSE estimate, under a prior determined by the observation \mathbf{y} and the distribution of the noise \mathbf{w} . If we assume that $\mathbf{y} = |\mathbf{z} + \mathbf{w}|$ with $\mathbf{w} \sim \mathcal{CN}(0, 1/\tau_w \mathbf{I})$, where \mathcal{CN} denotes a circular Gaussian distribution (real and imaginary components are i.i.d. with variance $\frac{1}{2}1/\tau_w$), this function, written elementwise, becomes

$$g_{z1,m}(\mathbf{p}_{1,m}, \tau_1) = \mathbb{E}[\mathbf{z}_{1,m}|\mathbf{y}_m, \mathbf{p}_{1,m}, \tau_w, \tau_1] = \left(\frac{\mathbf{y}_m^2}{1 + \tau_1/\tau_w} R_0\left(\frac{2\mathbf{y}_m|\mathbf{p}_{1,m}|}{1/\tau_w + 1/\tau_1}\right) + \frac{|\mathbf{p}_{1,m}|}{\tau_w/\tau_1 + 1} \right) \frac{\mathbf{p}_{1,m}}{|\mathbf{p}_{1,m}|}, \quad (10)$$

for indices $m = 1, \dots, M$, where $R_0(\cdot) \triangleq \frac{I_1(\cdot)}{I_0(\cdot)}$, where $I_0(\cdot)$ and $I_1(\cdot)$ denote zeroth and first order Bessel functions. This function, which is specific to the non-linearity $|\cdot|$, is what distinguishes prVAMP from other GVAMP algorithms. A derivation of this function and expression for its average partial derivative $\langle g'_{z1}(\cdot) \rangle$ can be found in [30].

2) *LMMSE Steps*: On lines 14 and 19 the algorithm performs MMSE estimation of \mathbf{x} and \mathbf{z} under the pseudo-priors that $\mathbf{r}_2 \sim \mathcal{CN}(\mathbf{x}, 1/\gamma_2)$ and $\mathbf{p}_2 \sim \mathcal{CN}(\mathbf{z}, 1/\tau_2)$, with $\Phi \mathbf{x} = \mathbf{z}$, using the functions $g_{x2}(\cdot)$ and $g_{z2}(\cdot)$. That is,

$$g_{x2}(\mathbf{r}_2, \mathbf{p}_2, \gamma_2, \tau_2) = \mathbb{E}[\mathbf{x}|\mathbf{r}_2, \mathbf{p}_2, \gamma_2, \tau_2],$$

and

$$g_{z2}(\mathbf{r}_2, \mathbf{p}_2, \gamma_2, \tau_2) = \mathbb{E}[\mathbf{z}|\mathbf{r}_2, \mathbf{p}_2, \gamma_2, \tau_2].$$

Because these estimates are linear with respect to \mathbf{r}_2 and \mathbf{p}_2 , these are called the LMMSE steps of the algorithm.

The LMMSE steps can be accelerated dramatically if one first computes a singular value decomposition (SVD) of the measurement matrix Φ , with $\Phi = \mathbf{U}\mathbf{S}\mathbf{V}^t$, before running the algorithm. With this decomposition in hand, the $g_{x2}(\cdot)$ and $g_{z2}(\cdot)$ functions can be written as

$$g_{x2}(\mathbf{r}_2, \mathbf{p}_2, \gamma_2, \tau_2) = \mathbf{V}\mathbf{D}_k(\tau_2 \mathbf{S}^t \mathbf{U}^t \mathbf{p}_2 + \gamma_2 \mathbf{V}^t \mathbf{r}_2), \quad (11)$$

where \mathbf{D}_k denotes an $n \times n$ diagonal matrix whose i^{th} diagonal entry is defined as $(\tau_2 \mathbf{s}_i^2 + \gamma_2)^{-1}$, where \mathbf{s}_i is the i^{th} singular value of Φ and

$$g_{z2}(\mathbf{r}_2, \mathbf{p}_2, \gamma_2, \tau_2) = \Phi g_{x2}(\mathbf{r}_2, \mathbf{p}_2, \gamma_2, \tau_2). \quad (12)$$

More information about these functions and expression for their average partial derivatives can be found in [28].

3) *Tuning and Initialization*: prVAMP is a Bayesian algorithm that requires priors on the distribution of the signal and noise. In this work, when reconstructing TMs, we used the following heuristic to estimate these quantities. We first computed an initial solution $\hat{\mathbf{x}}_{\text{GS}}$, using the Gerchberg-Saxton PR algorithm [34]. Then, treating this solution as the ground truth, we estimated the precisions as $\tau_w = \frac{1}{\|\mathbf{y} - |\Phi \hat{\mathbf{x}}_{\text{GS}}|\|^2}$ and $\tau_x = \frac{1}{\text{var}(\hat{\mathbf{x}}_{\text{GS}})}$. We assumed that both \mathbf{x} and \mathbf{w} were zero-mean. The same procedure was used for both the calibration and imaging steps; although we only imaged binary objects, this fact was not used as a prior within the algorithm.

When reconstructing TMs, we used the following heuristic to initialize prVAMP. Using the solution provided by GS, we set $\mathbf{r}_{10} = \hat{\mathbf{x}}_{\text{GS}}$, $\mathbf{p}_{10} = \Phi \hat{\mathbf{x}}_{\text{GS}}$, $\gamma_{10} = \frac{1}{\text{var}(\hat{\mathbf{x}}_{\text{GS}})}$, and $\tau_{10} = \frac{1}{\text{var}(\Phi \hat{\mathbf{x}}_{\text{GS}})}$.

4) *GPU Acceleration*: The prVAMP algorithm consists mostly of matrix-vector operations. By replacing these matrix-vector operations with matrix-matrix operations, we can solve thousands of phase retrieval problems in parallel. These matrix-matrix operations can be computed very efficiently using a GPU: Recovering 1000 rows of a $256^2 \times 64^2$ TM in sequence on an Intel 6800k CPU takes 300 minutes. Recovering these rows in parallel on a Pascal Titan X GPU takes 2 minutes.

To implement prVAMP we modified the original GVAMP Matlab code. Code demonstrating prVAMP on synthetic data is available within the GAMP project [35]. Code demonstrating prVAMP on experimental TM data, using GPU computing, is available on our website [36].

C. Measuring Intensity Transmission Matrices

To estimate the incoherent, real-valued intensity TM associated with a series of measurements $\mathbf{y}_p^2 = \mathbf{A}_{\text{intensity}} \mathbf{x}_p^2 + \epsilon_p$, we assembled the calibration data and the associated measurements into matrices \mathbf{X}^{2H} and \mathbf{Y}^{2H} (unlike the coherent model, no elementwise square root was taken). From there we first formed a maximum likelihood (ML) estimate of the intensity TM as

$$\mathbf{A}_{\text{intensity, ML}}^H = (\mathbf{X}^{2H})^\dagger \mathbf{Y}^{2H}, \quad (13)$$

where \dagger denotes pseudo-inverse.

Next, we assumed that the elements of \mathbf{A} and ϵ follow an i.i.d. Gaussian distribution with variances σ_a^2 , σ_ϵ^2 and estimated these variances using our ML solution: $\sigma_a^2 = \text{var}(\mathbf{A}_{\text{intensity, ML}})$ and $\sigma_\epsilon^2 = \frac{\|\mathbf{Y}^2 - \mathbf{A}_{\text{intensity, ML}} \mathbf{X}^2\|_F^2}{M}$. With these priors, the MAP estimate of \mathbf{A} becomes

$$\hat{\mathbf{A}}_{\text{intensity, MAP}}^H = \arg \max_{\mathbf{A}} \frac{-\|\mathbf{Y}^2 - \mathbf{A} \mathbf{X}^2\|_F^2}{\sigma_w^2} - \frac{\|\mathbf{A}\|_F^2}{\sigma_a^2}, \quad (14)$$

$$= (\mathbf{X} \mathbf{X}^H + \frac{\sigma_w^2}{\sigma_a^2} \mathbf{I})^{-1} \mathbf{X} \mathbf{Y}^H. \quad (15)$$

Because solving linear systems is much easier than solving phase retrieval problems, estimating $\mathbf{A}_{\text{intensity}}$ took a few minutes, as opposed to five hours.

We repeated an analogous process, forming an ML solution and then using this quantity to select the priors for our MAP solution, for imaging.

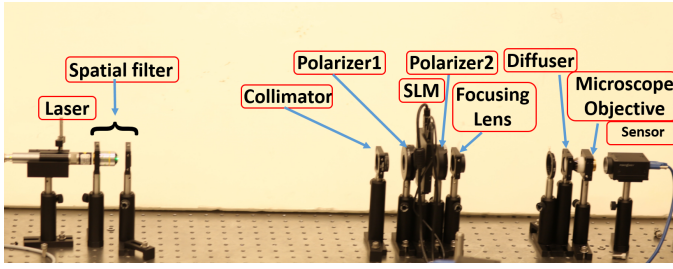


Fig. 3. Physical setup. A collimated laser beam illuminates a calibration pattern displayed on the spatial light modulator (SLM), the field from the SLM is focused onto the diffuser using the focusing lens, and the camera records the microscope objective (MO) magnified intensity pattern of the scattered light.

IV. EXPERIMENTAL SETUP

Our physical setup is illustrated in Figure 3. As shown in the figure, a spatially filtered and collimated laser beam illuminates a transmissive spatial light modulator (SLM) from Holoeye (LC 2012). This SLM operates in amplitude mode with a 1024×768 resolution⁴ and has 36 micrometer size square pixels. This SLM modulates the amplitude of the beam before the lens ($f = 150$ mm), which then focuses the light onto the scattering medium (a holographic 10 degree diffuser from Thorlabs). A microscope objective (Newport, X10, NA: 0.25) is then used to image the scattered light onto the sensor (Point Grey Grasshopper2, pixel size 6.45 micrometer).

To learn a TM under coherent illumination, we used a Z-Laser green focusable diode laser from Edmund Optics with wavelength $\lambda = 540$ nm, and for the partially incoherent experiments, we used a super-continuum laser source from NKT Photonics. With the latter laser, we were able to tune the wavelength bandwidth from anywhere between 10 nm and 100 nm. The corresponding coherence lengths range from roughly 12 micrometers to 1 micrometer. We also used a broadband LED light source, a Thorlabs M565L3, which is spatially as well as temporally incoherent.

In all the experiments, we captured $12 \cdot 64^2$ distinct 256×256 speckle images, y_1, \dots, y_p , where each speckle pattern corresponded to a distinct 64×64 calibration patterns, x_i , that was displayed on the SLM. The measurements were used to construct $256^2 \times 64^2$ TMs.

V. RESULTS AND DISCUSSION

In this section, we first demonstrate that with coherent illumination one can accurately measure a TM and image through a thick scatterer. We then demonstrate how reducing the coherence of the illumination changes the scattering processes and the properties of the associated TMs, which makes imaging through scattering more challenging.

A. Reconstruction Results Under Coherent Illumination

We begin by measuring a TM and imaging through a scattering media using a coherent illumination source. With coherent illumination, the double phase retrieval method combined with

⁴We display 64×64 patterns on the SLM by treating blocks of adjacent pixels as one large pixel.

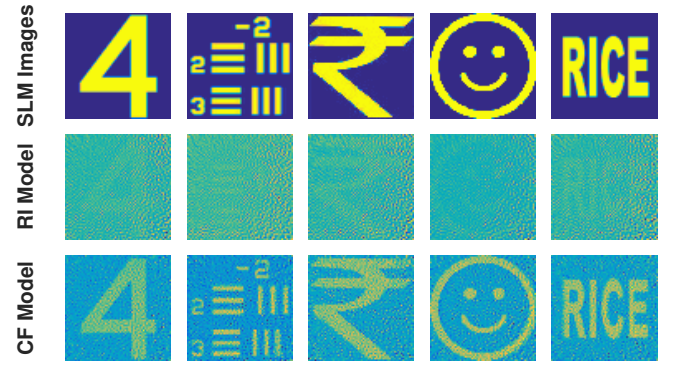


Fig. 4. Top: 64×64 SLM images. Middle: Reconstructions using real-valued intensity model (RI). Bottom: Reconstructions using complex-valued field (CF) model. For coherent laser illumination, the CF model (average structural similarity (SSIM) 0.26) produces high quality reconstructions whereas the RI model largely fails (average SSIM 0.01) [37].

GPU-accelerated prVAMP can effectively measure a complex-valued field TM and image through a scattering media, as demonstrated in Figure 4. The figure also presents reconstructions from a real-valued intensity model. With coherent illumination, the complex-field model's reconstructions are far superior to the real-intensity model's.

B. Results Under Partially Coherent Illumination

We now study the effects of coherence by replacing the laser diode; first with a tunable supercontinuum laser source and then with an incoherent LED. The tunable laser source was tested at bandwidths of 10 nm, 50 nm, and 100 nm.

1) *Speckle Contrast Decreases with Increasing Illumination Bandwidth:* Here we compare the speckle contrast of the scattered light produced by the various illumination sources, where speckle contrast is defined as

$$\text{contrast} = \frac{1}{I_{\text{mean}}} \sqrt{\frac{1}{N} \sum_{i=1}^N (I_i - I_{\text{mean}})^2} \quad (16)$$

$$I_{\text{mean}} = \frac{1}{N} \sum_{i=1}^N I_i. \quad (17)$$

The speckle patterns obtained, for the same SLM patterns, with different widths of broadband illumination are presented in Figure 5. The figure demonstrates that as one reduces the coherence of the light source the contrast of the speckle is reduced dramatically. In fact, for an incoherent LED source, the speckle is washed out almost entirely. A speckle contrast versus illumination bandwidth plot is shown in Figure 6. We see that speckle contrast decreases as the bandwidth increases and for the LED illumination it falls to only 0.8%. This result can be understood theoretically by interpreting the broadband illumination as the sum of many (almost) uncorrelated sources: With M uncorrelated sources the contrast would decrease as $1/\sqrt{M}$ [38]. Because of the spectral correlation bandwidth [20], the sources are not uncorrelated and the observed drop-off in contrast is not quite so swift.

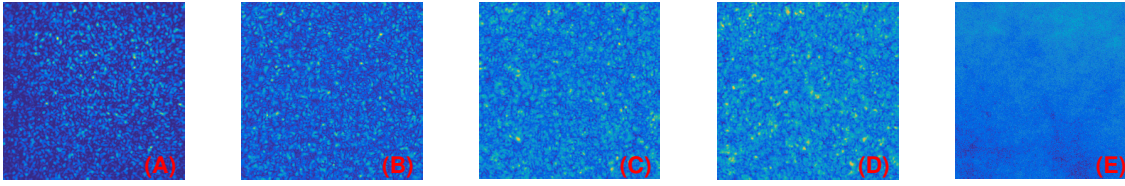


Fig. 5. Speckle patterns for different illumination types: (A) Coherent (B) 10nm, (C) 50nm, (D) 100nm, (E) incoherent LED. With increasing bandwidth the speckle size increases and contrast decreases. For incoherent LED illumination, speckle is washed out almost entirely.

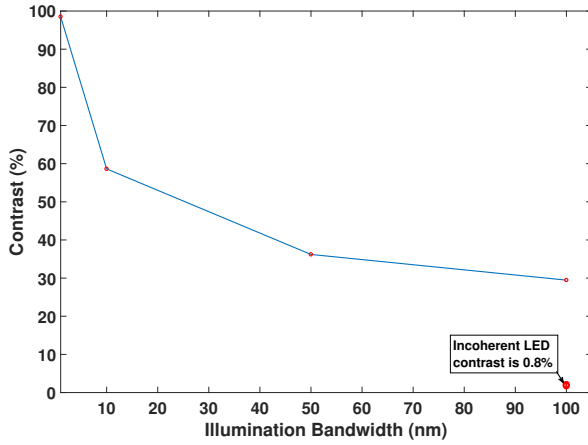


Fig. 6. Speckle contrast versus laser bandwidth. Increased bandwidth dramatically reduces the speckle contrast. Contrast for a spatially incoherent LED (100 nm bandwidth) drops to 0.8%.

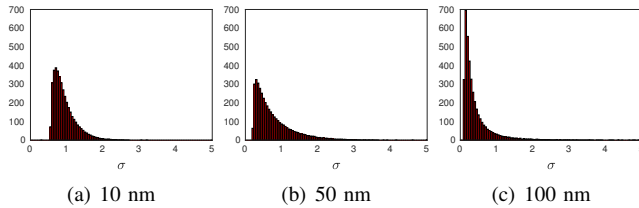


Fig. 7. Histograms of singular values for 10 nm, 50 nm, and 100 nm field-TMs. The singular values of the more broadband TMs are far more concentrated around zero.

C. Singular Values Decay with Increasing Illumination Bandwidth

In this section, we compare the singular values of the estimated complex-valued field TMs (TMs learned using the complex-valued field model) with the estimated real-valued intensity TMs (TMs learned using the real-valued intensity model).

The results, presented in Figures 7 and 8, demonstrate that as one increases the bandwidth of the illumination the singular values for both the complex-valued field TM and the real-valued intensity TM become concentrated around 0. The results also show that with 10 nm light the field TM has many large singular values, indicating that it is relatively easy to invert and should offer better reconstructions when used for imaging.

1) *Reconstruction Accuracy Declines with Increasing Illumination Bandwidth:* In Figure 9, we compare the imaging-

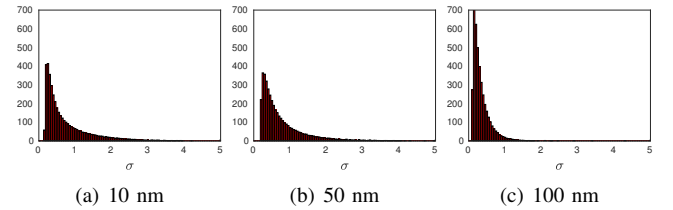


Fig. 8. Histograms of singular values for 10 nm, 50 nm, and 100 nm intensity-TMs. The singular values of the more broadband TMs are more concentrated around zero.

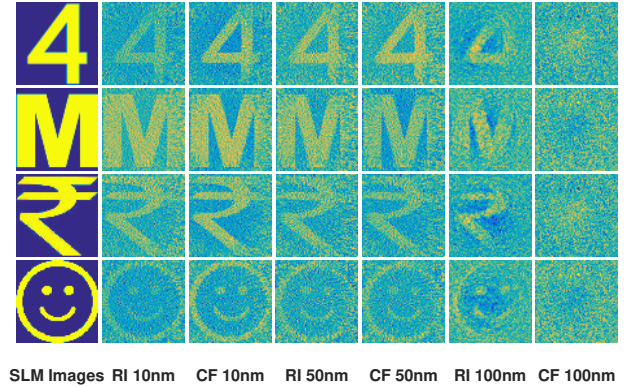


Fig. 9. Reconstruction results for 10nm, 50nm, 100nm illumination bandwidths using the complex-valued field (CF) model and the real-valued intensity (RI) model. With increasing illumination bandwidth, the CF model performance degrades and the RI model becomes competitive: For 10nm, 50nm, 100nm bandwidths, the average CF SSIMs are 0.22, 0.12, 0.00 and the RI SSIMs are 0.11, 0.09, 0.01.

through-scattering-media reconstructions as one varies the bandwidth of the illumination. The figure demonstrates that when dealing with narrow-band illumination, the complex-valued field (coherent) model is superior. However, as one increases the illumination bandwidth (i.e., decreases the coherence of the source), the complex-valued field model breaks down. In contrast, with increasing bandwidth the real-valued intensity (incoherent) model becomes competitive and at 100 nm bandwidth, it performs better than the complex-valued field model.

Returning to Figure 8, we can understand the reconstructions' behavior in terms of the singular values of the TMs. The singular values of the complex-field model start clustered near one and decay towards zero, whereas the real-intensity model's singular values remain clustered around zero for all bandwidths. Because linear systems are easier to invert,

as compared to solving phase retrieval problems, the real-intensity model is more robust to a poorly conditioned TM, with singular values near zero, and thus offers superior reconstructions in this regime.

VI. CONCLUSION

TMs are a powerful tool for imaging through, focusing light through, and understanding the properties of (static) multiple-scattering media. However, the complex-valued field model upon which the coherent TM models are based only holds true when dealing with completely coherent light sources. How this model breaks down under broadband illumination is poorly understood.

In this work, we have measured and studied TMs under illumination with varying bandwidths. We find that reducing the coherence of the illumination significantly reduces the information capacity of the scattering media: the TMs' singular values drop off quickly and the reconstructed images are less accurate. Simultaneously, we find that a real-valued intensity model can produce low-quality reconstructions across a host of different bandwidths.

The conclusions of this paper should be seen in light of the limitation that both aforementioned models are approximations under partially incoherent illumination. Generating more fitting models for partially incoherent illumination remains a future task.

To perform the high-resolution reconstructions presented in this work, we have developed a new, GPU-accelerated algorithm called prVAMP. Using this algorithm, high-resolution TMs can be reconstructed in only a few hours. The datasets described in this work have been made available on our website [36].

Acknowledgments

We would like to thank all anonymous reviewers for their tremendously useful comments to help improve our work. Thanks to Phil Schniter for suggesting we extend GVAMP to prVAMP and for helping us tune the algorithm. Thanks also to Laurent Daudet and Boshra Rajaei for sharing their prSAMP code.

This work was supported by REVEAL grant HR0011-16-C-0028, ARO grants W911NF-12-1-0407 and W911NF-15-1-0316, ONR grants N00014-15-1-2735, N00014-15-1-2735, N00014-17-1-2551, and N00014-18-12571, AFOSR grant FA9550-14-1-0088, and DARPA grant G001534-7500. In addition, Christopher Metzler was supported by the NSF GRF program and NASA TSGC, Richard Baraniuk was supported by the DoD Vannevar Bush Faculty Fellowship (NSSEFF) grant N00014-18-1-2047, and Oliver Cossairt and Ashok Veeraghavan were supported by NSF Career grants IIS-1453192 and IIS-1652633, respectively.

APPENDIX A

A COMPARISON OF PHASE RETRIEVAL ALGORITHMS

In this section, we compare the performance of prVAMP with fifteen other phase retrieval algorithms. We test the algorithms under three conditions: (1) with high signal-to-noise

ratio (SNR) Gaussian measurements, (2) with high SNR binary measurements, and (3) with low SNR binary measurements.

The results show that most algorithms work reasonably well with Gaussian measurements. However, when dealing with binary measurements many algorithms fail to reconstruct the signal. In the binary regime, prVAMP and prSAMP offer by far the best performance.

In all three tests, we use the following signal model

$$\mathbf{y} = |\mathbf{Ax} + \mathbf{w}|,$$

where $\mathbf{A} \in \mathbb{C}^{m \times n}$ or $\mathbf{A} \in \{0, 1\}^{m \times n}$ and $\mathbf{w} \sim \mathcal{CN}(0, \sigma^2 \mathbf{I})$. Note that we have added noise before the nonlinearity.

For all three tests $x \sim \mathcal{CN}(0, \mathbf{I})$ and we define SNR as

$$\text{SNR} = \frac{\|\mathbf{Ax}\|}{\|\mathbf{w}\|}.$$

Except for the recovery time results in Section A-D, where we sweep across a host of signal dimensions, we fix $n = 128$. That is $\mathbf{x} \in \mathbb{C}^{128}$.

We report recovery accuracy in terms of median, disambiguated, normalized mean squared error (NMSE) over 11 trials. By disambiguated, we mean that we have corrected for the global phase ambiguity and, in the case of real-valued measurement matrices, the conjugation ambiguity as well.

We used our own implementations of prVAMP and prGAMP [30], which were derived from code in the Gamp-Matlab toolbox [35]. We used the original authors' implementations of prSAMP [26] and prVBEM [39]. The implementations of Gerchberg-Saxton (GS) [34], Fienup's HIO algorithm [43], Amplitude Flow (AF) [46], [47], Reweighted Amplitude Flow (RAF) [44], Truncated Amplitude Flow (TAF) [47], Wirtinger Flow (WF) [40], Reweighted Wirtinger Flow (RAF) [45], Truncated Wirtinger Flow (TAF) [50], Kaczmarz [48], PhaseLamp [49], PhaseLift [41], and PhaseMax [42], as well as much of the support code that we used to generate these results, comes from PhasePack [46]. We modified the original PhasePack implementation of GS so as to use the pseudo-inverse of the measurement matrix, rather than a least-squares solver at each iteration. Except for the number of iterations, which were fixed at 200 for all algorithms, implementation details were left unchanged.

Initial versions of these results were first presented in [23].

A. High SNR Gaussian Measurements

As a point of reference, we first compare the various algorithms with i.i.d. circular-Gaussian distributed measurement matrices with an SNR of 50. Presented in Figure 10, these results show that almost all phase retrieval algorithms operate well in this regime.⁵ The results also demonstrate that prGAMP and prSAMP can reconstruct the signal using fewer measurements than competing methods; they succeed around $m = 2.2n$. These algorithms are closely followed by prVAMP and prVBEM which reconstruct the signal for $m \geq 2.5n$. AF, TAF, WF, and TWF are also close behind.

⁵If run for more iterations (> 1000) Kaczmarz also works with Gaussian measurements.

These findings are consistent with theoretical results from [52], which proves that with Gaussian measurements a related version of AMP [53] will solve the phase retrieval with high probability for $m \gtrsim 2.48n$ and will solve the problem depending on the initialization for $2n \leq m \lesssim 2.48n$.

B. High SNR Binary Measurements

To illustrate the difficulty posed by binary measurement matrices, we conduct the same test as before but with binary, Bernoulli $p = .5$ distributed measurements, again with an SNR of 50. Presented in Figure 11, these results show that, even with high SNR measurements, many phase retrieval algorithms struggle in this regime; prGAMP, Kaczmarz, PhaseLamp, and PhaseMax performs especially poorly. In this regime, prVAMP offers a sharp phase transition at $m = 3n$.⁶ prSAMP also works for $m \geq 3n$, but it also sometimes succeeds for $m \leq 3n$. No other phase retrieval algorithms are competitive.

C. Low SNR Binary Measurements

Finally, we test the algorithms with noisy (SNR = 10) binary measurements, which model the phase retrieval problems associated with learning a TM. Presented in Figure 12, these results show that this problem is especially challenging. prVAMP and prSAMP again offer the best performance. Note however that with enough measurements prVBEM, Fienup, GS, and RWF start to work reasonably well.

D. Computation Times

Here we report the computation times of the algorithms on problems of varying dimension. All results were recorded on an Intel 6800K CPU.

Table I compares the reconstruction times of the various phase retrieval algorithms when solving $m = 12n$ oversampled, high SNR phase retrieval problems with complex Gaussian measurement matrices. The results show that with high dimensional problems, prVAMP runs hundreds of times faster than prSAMP.

Table I does not include computation times associated with preprocessing operations. prVAMP and GS perform an economical SVD and a pseudoinverse, respectively, of the measurement matrix. The computations times associated with these operations are presented in Table II. In the context of double phase retrieval, these operations have a negligible effect on the overall runtime because they can be done once and then reused tens of thousands of times for different problems.

E. Parameter Settings

The prVAMP, prSAMP, prVBEM, and prGAMP algorithms are all Bayesian and as such use information about the distribution of the signal and noise. In this work we set these parameters by hand, but techniques exist to estimate these parameters automatically [51], [30], [39]. Table III presents the parameters used with the various algorithms during simulation.

⁶The phase transition is the minimum amount of oversampling required such that the algorithms succeed with high probability.

Algorithm	$n = 64$	$n = 256$	$n = 1024$
prVAMP	0.12	0.38	5.46
prSAMP	4.26	67.57	1044.07
prVBEM	0.16	0.89	26.91
prGAMP	0.04	0.19	4.38
WF	0.02	0.11	3.11
RWF	0.05	0.24	7.45
TWF	0.05	0.15	5.32
Kaczmarz	0.02	0.05	1.20
AF	0.02	0.09	3.61
RWF	0.03	0.15	4.48
TAF	0.03	0.11	5.35
PhaseLamp	0.18	1.02	47.58
Fienup	0.05	0.40	10.05
GS	0.04	0.32	7.81
PhaseLift	1.38	27.67	792.98
PhaseMax	0.07	0.27	6.10

TABLE I
RUNNING TIMES (IN SECONDS) OF VARIOUS PHASE RETRIEVAL ALGORITHMS WITH $12 \cdot N \times N$ OVERSAMPLED MEASUREMENTS AT VARIOUS RESOLUTIONS. ALL ALGORITHMS ARE RUN FOR 200 ITERATIONS.

Preprocessing Step	$n = 64$	$n = 256$	$n = 1024$
Economical SVD	0.008	0.12	2.4
Pseudoinverse	0.59	0.62	2.9

TABLE II
THE COMPUTATION TIMES (IN SECONDS) OF ONE-TIME PREPROCESSING OPERATIONS ASSOCIATED WITH $m = 12n$ MEASUREMENT MATRICES. prVAMP REQUIRES AN ECONOMICAL SVD OF THE MEASUREMENT MATRIX AND GS REQUIRES A PSEUDOINVERSE OF THE MEASUREMENT MATRIX. THESE VALUES CAN THEN BE REUSED FOR ALL PHASE RETRIEVAL PROBLEMS USING THE SAME MEASUREMENT MATRIX.

The other algorithms, which are not Bayesian, did not use signal priors. Their parameters were kept at the default values from [46].

For simulations with Gaussian measurement matrices, all algorithms used the optimal spectral initializer from [54]. For simulations with Binary measurement matrices, all algorithms were provided a random initialization, $x_o \sim \mathcal{CN}(0, \mathbf{I})$. With binary measurement matrices, the spectral initializer did not work, and in fact produced worse results than random initializations.

When reconstructing TMs from experimental measurements, GS was provided a random initialization and its solution was used to initialize and set the parameters for prVAMP.

APPENDIX B PHASE RETRIEVAL WITH FAST, BLOCK-DIAGONAL MEASUREMENT MATRICES

The fast phase retrieval method proposed in [26] works as follows. First, a series of measurements are captured with a block-diagonal measurement matrix. Next one solves an independent phase retrieval subproblem for each of these k blocks; each resulting solution, $\hat{x}_1, \hat{x}_2, \dots, \hat{x}_k$ will have an unknown and unique global phase ambiguity, $e^{j\theta_1}, e^{j\theta_2}, \dots, e^{j\theta_k}$.⁷ Finally, by capturing a small number of additional measurements, one can setup an additional, k -dimensional phase retrieval problem

⁷When the measurement matrix is real-valued, a conjugation ambiguity appears as well.

Algorithm	Signal Priors	Other Parameters
prVAMP	Signal mean and variance and noise variance	Signal damping = .8, Variance damping = .5
prSAMP	Signal mean and variance and noise variance	Damping = .8
prVBEM	Noise variance, otherwise defaults	Defaults
prGAMP	Signal mean and variance and noise variance	Damping = .8

TABLE III

THE PARAMETERS USED FOR TESTING THE AMP-BASED PHASE RETRIEVAL ALGORITHMS IN SIMULATION. THE OTHER ALGORITHMS DID NOT USE SIGNAL PRIORS AND USED THEIR DEFAULT PARAMETERS FROM [46].

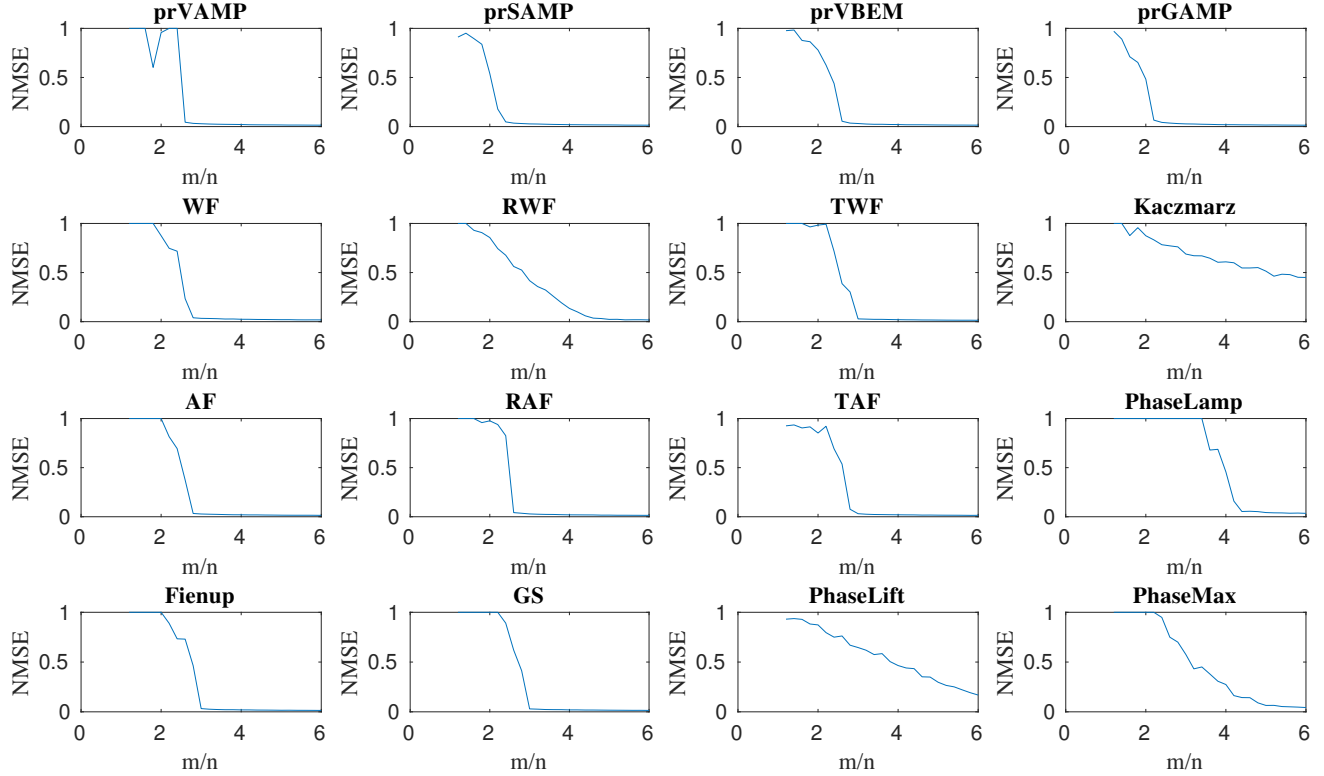


Fig. 10. High SNR Gaussian measurement matrices recovery accuracies. With enough samples, most phase retrieval algorithms are effective in this regime.

to estimate these global phase shifts and remove them to compute the overall solution; $\hat{\mathbf{x}} = [\hat{\mathbf{x}}_1^t e^{-j\theta_1}, \hat{\mathbf{x}}_2^t e^{-j\theta_2}, \dots, \hat{\mathbf{x}}_k^t e^{-j\theta_k}]^t$.

We tested prVAMP and prSAMP at a number of different resolutions using both dense and block-diagonal measurement matrices. For all tests, the SNR was 10 and the oversampling rate ($\frac{m}{n}$) was 6. For input dimensions of 2^6 , 2^7 , 2^8 , 2^9 , 2^{10} , 2^{11} , and 2^{12} , we split the measurement matrix into 4, 4, 8, 16, or 32 blocks, respectively, as suggested in [27]. The non-zero elements of our measurement matrices were drawn from a circularly symmetric complex Gaussian distribution.

The associated reconstruction times and NMSE's are presented in Figure 13. They show that at these (not extremely high) resolutions, prVAMP with dense matrices is still faster than prSAMP with the block matrices. prVAMP with block matrices is faster still. Using block matrices with either algorithm produces a small increase in NMSE. Note that at higher resolutions, especially when a dense measurement matrix could no longer be stored in memory, using block matrices would be more beneficial. All these results were on a CPU, but prVAMP can easily be mapped onto a GPU for

further acceleration.

APPENDIX C

IMAGING PERFORMANCE AS A FUNCTION OF SAMPLING RATE

All the previous reconstruction results used 256×256 camera pixels to reconstruct 64×64 SLM pixels, for an effective sampling rate of $\frac{m}{n} = 16$. As one reduces the sampling rate, one expects the reconstruction accuracy to deteriorate. In Figure 14 we provide intensity-based and field-based reconstructions at sampling rates of $\frac{m}{n} = 12$, $\frac{m}{n} = 2$, and $\frac{m}{n} = 1$ when the illumination bandwidth is 10 nm. Somewhat surprisingly, both the field-based reconstructions and the intensity-based reconstructions suffer about equally from low sampling rates (though the field-based reconstructions do suffer marginally more).

REFERENCES

- [1] M. Minsky, "Microscopy apparatus: Us, 3013467."
- [2] M. Minsky, "Memoir on inventing the confocal scanning microscope," *Scanning*, vol. 10, no. 4, pp. 128–138, 1988.

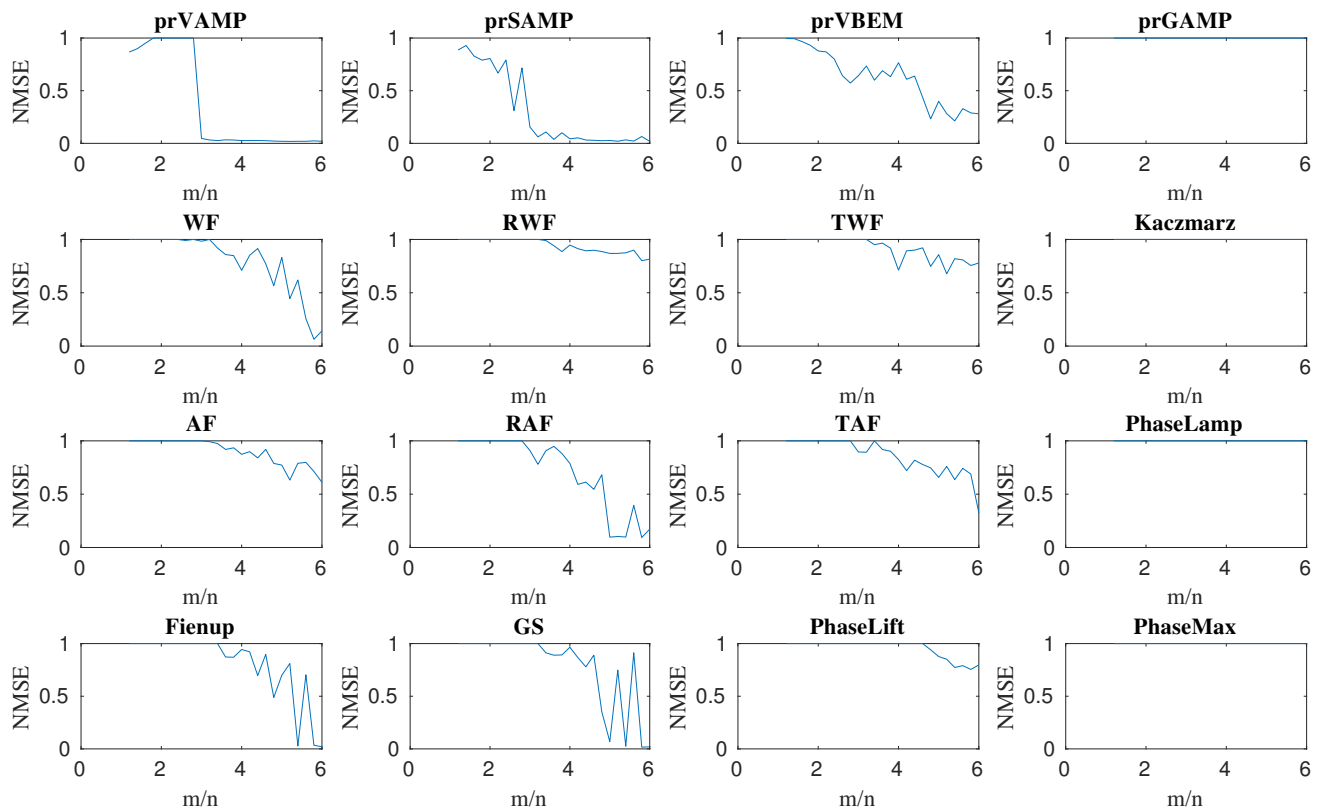


Fig. 11. High SNR binary measurement matrices recovery accuracies. Many phase retrieval algorithms fail in this regime. prSAMP and prVAMP offer the best phase transition.

- [3] C. Dunsby and P. French, "Techniques for depth-resolved imaging through turbid media including coherence-gated imaging," *Journal of Physics D: Applied Physics*, vol. 36, no. 14, p. R207, 2003.
- [4] R. Tadano, A. Kumar Pediredla, and A. Veeraraghavan, "Depth selective camera: A direct, on-chip, programmable technique for depth selectivity in photography," in *Proceedings of the IEEE International Conference on Computer Vision*, pp. 3595–3603, 2015.
- [5] A. Velten, T. Willwacher, O. Gupta, A. Veeraraghavan, M. G. Bawendi, and R. Raskar, "Recovering three-dimensional shape around a corner using ultrafast time-of-flight imaging," *Nature Communications*, vol. 3, p. 745, 2012.
- [6] N. Naik, S. Zhao, A. Velten, R. Raskar, and K. Bala, "Single view reflectance capture using multiplexed scattering and time-of-flight imaging," in *ACM Transactions on Graphics (TOG)*, vol. 30, p. 171, ACM, 2011.
- [7] F. Heide, M. B. Hullin, J. Gregson, and W. Heidrich, "Low-budget transient imaging using photonic mixer devices," *ACM Transactions on Graphics (TOG)*, vol. 32, no. 4, p. 45, 2013.
- [8] A. Kanaev, A. Watnik, D. Gardner, C. Metzler, K. Judd, P. Lebow, K. Novak, and J. Lindle, "Imaging through extreme scattering in extended dynamic media," *Optics Letters*, vol. 43, no. 13, pp. 3088–3091, 2018.
- [9] X. Ma, W. Xiao, and F. Pan, "Optical tomographic reconstruction based on multi-slice wave propagation method," *Optics Express*, vol. 25, no. 19, pp. 22595–22607, 2017.
- [10] L. Tian and L. Waller, "3d intensity and phase imaging from light field measurements in an led array microscope," *Optica*, vol. 2, no. 2, pp. 104–111, 2015.
- [11] U. S. Kamilov, I. N. Papadopoulos, M. H. Shoreh, A. Goy, C. Vonesch, M. Unser, and D. Psaltis, "Learning approach to optical tomography," *Optica*, vol. 2, no. 6, pp. 517–522, 2015.
- [12] Y. Wu, M. K. Sharma, and A. Veeraraghavan, "Wish: wavefront imaging sensor with high resolution," *Light: Science & Applications*, vol. 8, no. 1, p. 44, 2019.
- [13] J. Holloway, Y. Wu, M. K. Sharma, O. Cossairt, and A. Veeraraghavan, "Savi: Synthetic apertures for long-range, subdiffraction-limited visible imaging using fourier ptychography," *Science advances*, vol. 3, no. 4, p. e1602564, 2017.
- [14] J. Holloway, M. S. Asif, M. K. Sharma, N. Matsuda, R. Horstmeyer, O. Cossairt, and A. Veeraraghavan, "Toward long-distance subdiffraction imaging using coherent camera arrays," *IEEE Transactions on Computational Imaging*, vol. 2, no. 3, pp. 251–265, 2016.
- [15] J. Bertolotti, E. G. van Putten, C. Blum, A. Legendijk, W. L. Vos, and A. P. Mosk, "Non-invasive imaging through opaque scattering layers," *Nature*, vol. 491, no. 7423, p. 232, 2012.
- [16] O. Katz, P. Heidmann, M. Fink, and S. Gigan, "Non-invasive single-shot imaging through scattering layers and around corners via speckle correlations," *Nature Photonics*, vol. 8, no. 10, pp. 784–790, 2014.
- [17] S. Popoff, G. Lerosey, M. Fink, A. C. Boccarda, and S. Gigan, "Image transmission through an opaque material," *Nature communications*, vol. 1, p. 81, 2010.
- [18] T. Chaigne, O. Katz, A. C. Boccarda, M. Fink, E. Bossy, and S. Gigan, "Controlling light in scattering media non-invasively using the photoacoustic transmission matrix," *Nature Photonics*, vol. 8, no. 1, p. 58, 2014.
- [19] B. Rajaei, E. W. Tramel, S. Gigan, F. Krzakala, and L. Daudet, "Intensity-only optical compressive imaging using a multiply scattering material and a double phase retrieval approach," in *2016 IEEE International Conference on Acoustics, Speech and Signal Processing (ICASSP)*, pp. 4054–4058, March 2016.
- [20] D. Andreoli, G. Volpe, S. Popoff, O. Katz, S. Grésillon, and S. Gigan, "Deterministic control of broadband light through a multiply scattering medium via the multispectral transmission matrix," *Scientific reports*, vol. 5, p. 10347, 2015.
- [21] M. Mounaix, D. Andreoli, H. Defienne, G. Volpe, O. Katz, S. Grésillon, and S. Gigan, "Spatiotemporal coherent control of light through a multiple scattering medium with the multispectral transmission matrix," *Physical review letters*, vol. 116, no. 25, p. 253901, 2016.
- [22] A. Drémeau, A. Liutkus, D. Martina, O. Katz, C. Schülke, F. Krzakala, S. Gigan, and L. Daudet, "Reference-less measurement of the transmission matrix of a highly scattering material using a dmd and phase retrieval techniques," *Opt. Express*, vol. 23, pp. 11898–11911, May 2015.

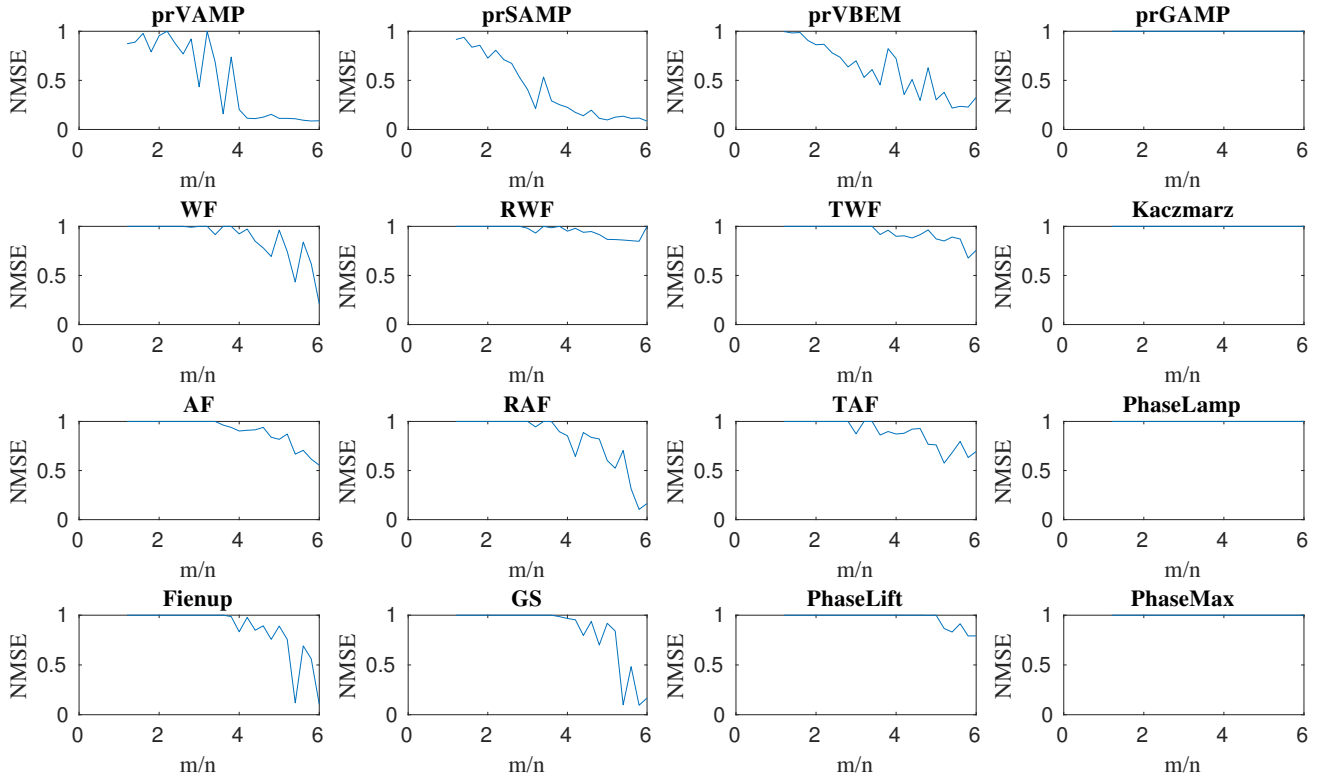


Fig. 12. Low SNR binary measurement matrices recovery accuracies. This problem is especially challenging. At sampling rates of 5, only prSAMP and prVAMP offer even reasonable recovery accuracies.

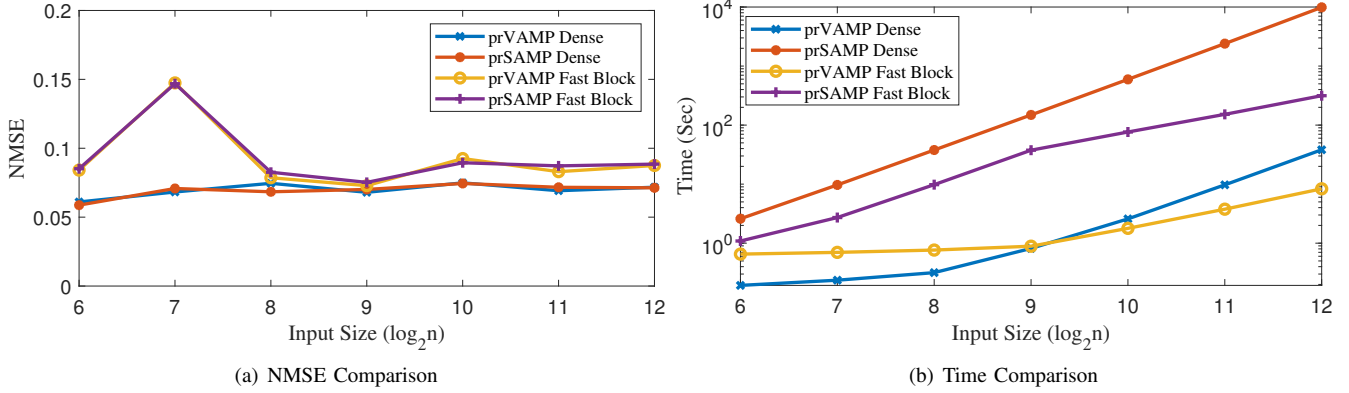


Fig. 13. Comparison between prVAMP and prSAMP with and without fast block-diagonal measurement matrices. Both algorithms can use block-diagonal measurement matrices to trade off a little performance for reduced run-times.

- [23] C. A. Metzler, M. K. Sharma, S. Nagesh, R. G. Baraniuk, O. Cossairt, and A. Veeraraghavan, "Coherent inverse scattering via transmission matrices: Efficient phase retrieval algorithms and a public dataset," in *Computational Photography (ICCP), 2017 IEEE International Conference on*, pp. 1–16, IEEE, 2017.
- [24] S. Popoff, G. Lerosey, R. Carminati, M. Fink, A. Boccarda, and S. Gigan, "Measuring the transmission matrix in optics: an approach to the study and control of light propagation in disordered media," *Physical Review Letters*, vol. 104, no. 10, p. 100601, 2010.
- [25] J. Yoon, K. Lee, J. Park, and Y. Park, "Measuring optical transmission matrices by wavefront shaping," *Optics Express*, vol. 23, no. 8, pp. 10158–10167, 2015.
- [26] B. Rajaei, S. Gigan, F. Krzakala, and L. Daudet, "Robust phase retrieval with the swept approximate message passing (prsamp) algorithm," *Image Processing On Line*, vol. 7, pp. 43–55, 2017.
- [27] B. Rajaei, S. Gigan, F. Krzakala, and L. Daudet, "Fast phase retrieval for high dimensions: A block-based approach," *IEEE Signal Processing Letters*, vol. 23, no. 9, pp. 1179–1182, 2016.
- [28] P. Schniter, S. Rangan, and A. K. Fletcher, "Vector approximate message passing for the generalized linear model," in *Signals, Systems and Computers, 2016 50th Asilomar Conference on*, pp. 1525–1529, IEEE, 2016.
- [29] S. Rangan, "Generalized approximate message passing for estimation with random linear mixing," in *Information Theory Proceedings (ISIT), 2011 IEEE International Symposium on*, pp. 2168–2172, IEEE, 2011.
- [30] P. Schniter and S. Rangan, "Compressive phase retrieval via generalized approximate message passing," *IEEE Transactions on Signal Processing*, vol. 63, no. 4, pp. 1043–1055, 2015.
- [31] S. Boyd, N. Parikh, E. Chu, B. Peleato, J. Eckstein, et al., "Distributed optimization and statistical learning via the alternating direction method of multipliers," *Foundations and Trends in Machine Learning*, vol. 3, no. 1, pp. 1–122, 2011.
- [32] F. Caltagirone, L. Zdeborová, and F. Krzakala, "On convergence of approximate message passing," in *2014 IEEE International Symposium*

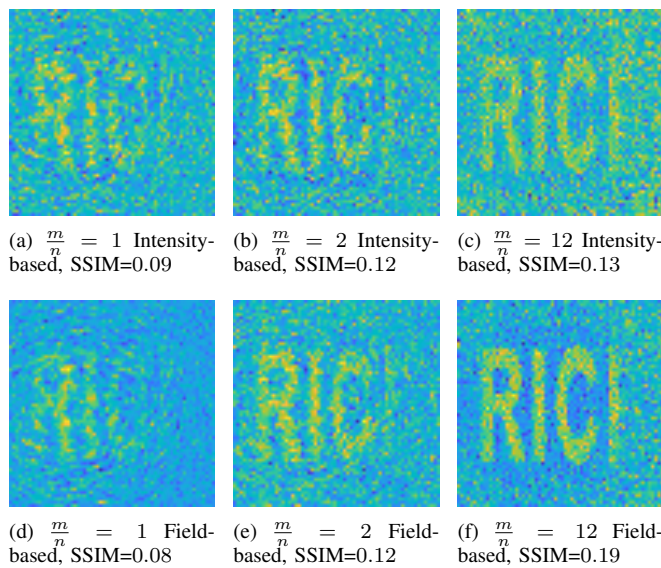


Fig. 14. Comparison between field-based reconstructions and intensity-based reconstructions for 10nm bandwidth at a variety of sampling rates. Both models benefit from higher sampling rates.

on *Information Theory*, pp. 1812–1816, IEEE, 2014.

[33] S. Rangan, P. Schniter, and A. Fletcher, “On the convergence of approximate message passing with arbitrary matrices,” in *2014 IEEE International Symposium on Information Theory*, pp. 236–240, IEEE, 2014.

[34] R. W. Gerchberg, “A practical algorithm for the determination of phase from image and diffraction plane pictures,” *Optik*, vol. 35, p. 237, 1972.

[35] “GampMatlab Toolbox.” http://gampmatlab.wikia.com/wiki/Generalized_Approximate_Message_Passing.

[36] “Transmission matrix dataset.” <http://dsp.rice.edu/research/transmissionmatrices/>.

[37] Z. Wang, A. C. Bovik, H. R. Sheikh, E. P. Simoncelli, *et al.*, “Image quality assessment: from error visibility to structural similarity,” *IEEE transactions on image processing*, vol. 13, no. 4, pp. 600–612, 2004.

[38] J. W. Goodman, “Some fundamental properties of speckle,” *JOSA*, vol. 66, no. 11, pp. 1145–1150, 1976.

[39] A. Drémeau and F. Krzakala, “Phase recovery from a bayesian point of view: the variational approach,” in *2015 IEEE International Conference on Acoustics, Speech and Signal Processing (ICASSP)*, pp. 3661–3665, IEEE, 2015.

[40] E. J. Candes, X. Li, and M. Soltanolkotabi, “Phase retrieval via wirtinger flow: Theory and algorithms,” *IEEE Transactions on Information Theory*, vol. 61, no. 4, pp. 1985–2007, 2015.

[41] E. J. Candes, T. Strohmer, and V. Voroninski, “Phaselift: Exact and stable signal recovery from magnitude measurements via convex programming,” *Communications on Pure and Applied Mathematics*, vol. 66, no. 8, pp. 1241–1274, 2013.

[42] T. Goldstein and C. Studer, “Phasemax: Convex phase retrieval via basis pursuit,” *IEEE Transactions on Information Theory*, 2018.

[43] J. R. Fienup, “Reconstruction of an object from the modulus of its fourier transform,” *Optics letters*, vol. 3, no. 1, pp. 27–29, 1978.

[44] G. Wang, G. B. Giannakis, Y. Saad, and J. Chen, “Solving Almost all Systems of Random Quadratic Equations,” *ArXiv e-prints*, May 2017.

[45] Z. Yuan and H. Wang, “Phase retrieval via reweighted wirtinger flow,” *Applied optics*, vol. 56, no. 9, pp. 2418–2427, 2017.

[46] R. Chandra, Z. Zhong, J. Hontz, V. McCulloch, C. Studer, and T. Goldstein, “Phasepack: A phase retrieval library,” *Asilomar Conference on Signals, Systems, and Computers*, 2017.

[47] G. Wang, G. B. Giannakis, and Y. C. Eldar, “Solving systems of random quadratic equations via truncated amplitude flow,” *IEEE Transactions on Information Theory*, vol. 64, no. 2, pp. 773–794, 2018.

[48] K. Wei, “Solving systems of phaseless equations via kaczmarz methods: A proof of concept study,” *Inverse Problems*, vol. 31, no. 12, p. 125008, 2015.

[49] O. Dhifallah, C. Thrampoulidis, and Y. M. Lu, “Phase retrieval via linear programming: Fundamental limits and algorithmic improvements,” in

Communication, Control, and Computing (Allerton), 2017 55th Annual Allerton Conference on, pp. 1071–1077, IEEE, 2017.

[50] Y. Chen and E. Candes, “Solving random quadratic systems of equations is nearly as easy as solving linear systems,” in *Advances in Neural Information Processing Systems*, pp. 739–747, 2015.

[51] C. A. Metzler, P. Schniter, and R. G. Baraniuk, “An expectation-maximization approach to tuning generalized vector approximate message passing,” in *International Conference on Latent Variable Analysis and Signal Separation*, pp. 395–406, Springer, 2018.

[52] J. Ma, J. Xu, and A. Maleki, “Approximate message passing for amplitude based optimization,” *Proceedings of the 35th International Conference on Machine Learning*, vol. 80, pp. 3365–3374, 2018.

[53] D. L. Donoho, A. Maleki, and A. Montanari, “Message-passing algorithms for compressed sensing,” *Proceedings of the National Academy of Sciences*, vol. 106, no. 45, pp. 18914–18919, 2009.

[54] M. Mondelli and A. Montanari, “Fundamental limits of weak recovery with applications to phase retrieval,” *arXiv preprint arXiv:1708.05932*, 2017.